Turbulence Kinetic Energy Dissipation Rate Estimate for a Low-Level Jet with Doppler Lidar Data: A Case Study

CASSIA M. L. BEU[a] AND EDUARDO LANDULFO[a]

[a] *Instituto de Pesquisas Energeticas e Nucleares, Sao Paulo, Brazil*

(Manuscript received 19 November 2020, in final form 10 February 2022)

ABSTRACT: Low-level jets are a recurrent feature of our study area in Ipero municipality of southeastern Brazil. They grow very near the surface as shown by this case study. These two aspects increase the needs for a realistic modeling of the low-level jet to simulate the atmospheric dispersion of industrial emissions. In this concern, we applied a recently proposed technique to estimate the turbulence kinetic energy dissipation rate of a low-level jet case with Doppler lidar data. This low-level jet remained for its entire lifetime (around 12 h) within a shallow layer (under 300 m); beyond this, we did not notice a remarkable directional shear as in other studies. Even for a shallow layer as for this study case, we observed strong spatiotemporal variability of the turbulence kinetic energy dissipation rate. We also detected a channel connecting the layers above and below the low-level jet that may be an exchange channel of their properties.

KEYWORDS: Atmosphere–land interaction; Boundary layer; Jets; Kinetic energy; Lidars/lidar observations

1. Introduction

The energy dissipation rate ϵ is one of the terms of the turbulence kinetic energy (TKE) budget equation; ϵ indicates the turbulence strength, which means it is usually higher where the TKE production is higher (Stull 1988). Conceptual models assume that the TKE and the ϵ are stronger near the surface for stable and near-neutral planetary boundary layer (PBL), but the maximum TKE and ϵ are located at higher levels for the unstable PBL (Stull 1988). However, some relatively more recent studies have shown that under low-level jets (LLJ) presence these conceptual models are not valid anymore (Banta et al. 2006; Bonin et al. 2015; Deb Burman et al. 2018). Hereinafter, we use the term LLJ just for the maximum wind stream observed within the PBL, although the same term is also used for a typical atmospheric feature of the South America circulation (Nobre et al. 2013) that occurs around 850 hPa and is beyond the scope of this study.

The LLJs produce diverse economic and social impacts on our lives, which include pollutant and moisture transport and dispersion, forest fire propagation, flight safety and wind power production (Bodini et al. 2018b). Some studies have identified the LLJ role for the pollutant transport. There was the case of the persistent Baltimore, Maryland, LLJ (lasting 10 h, approximately) that caused the entrainment of photochemical ozone (O_3) (from the residual layer) to the stable boundary layer and then transported the O_3 downwind (Sullivan et al. 2017). Another case of transport of photochemical O_3 associated with the LLJ was documented by Banta et al. (1998). The O_3 produced at the urban area was transported to the rural zone of Nashville, Tennessee, during a stagnation episode. At Bordj-Badji Mokhtar (in the Sahara central region of Algeria), the LLJs are responsible for the dust transport due to the mix-down of momentum (Allen and Washington 2014). The authors also highlighted other papers related to the dust emission by the LLJs over desertic regions. Jia et al. (2016) concluded that the LLJ turbulence transported aerosols and moisture vertically from the surface to the residual layer in their Hampton, Virginia, experiment. Besides that, they also found that the cloud formation is associated with the LLJ presence. At the Great Salt Lake in Utah, the pollutants are transported out of the city by the LLJs if the thermally forced flow is short lived or absent (Darby et al. 2006). As we see from those few examples, the LLJ impacts on pollution dispersion and air quality are diverse.

Figure 1 from Banta et al. (2006) illustrates the vertical profile of the TKE and the vertical turbulent transport of TKE for what they called a traditional boundary layer (without LLJ) and an "*upside down*" boundary layer (with LLJ). According to their illustrative scheme, under LLJ presence, the turbulence is transported downward from a primary source aloft in the boundary layer. Even if a clear night with radiational cooling, strong inversion, and strong surface-based stability is the ideal environment for the LLJ development and vertical transport of TKE, stability can be more or less strong, as shown in Bonin et al. (2015). Bonin et al. (2015) also noticed that the turbulence and thermodynamics characteristics of the nocturnal boundary layer are different for the southerly and northerly LLJs from the LABLE-I campaign that took place at Oklahoma. Analyzing only the southerly LLJs, Bonin et al. (2015) realized that cases with moderate and strong turbulence profiles exhibit features of a weakly stable boundary layer, while those with weak turbulence tend to resemble the very stable boundary layer. Besides that, they found that turbulence is generated near the surface and transported upward when the turbulence intensity is large. When the mixing is weak, turbulence is generated either near the surface (and transported upward) or aloft (and transported downward) depending on whether an "*upside down*" or

Corresponding author: Cassia M. L. Beu, cassia.beu@gmail.com

Earth Interactions is published jointly by the American Meteorological Society, the American Geophysical Union, and the Association of American Geographers.

DOI: 10.1175/EI-D-20-0027.1

traditional boundary layer is present. Within the moderate turbulence regime, the turbulence is generated both at surface (and transported upward) and near the wind speed maximum (and transported downward). The LLJ observed during the Indian summer monsoon also produced downward transport of turbulence (Deb Burman et al. 2018). The downward turbulence peaks coincide with strong vertical shear and can cause intermittent events at the surface, as enhancement of fluxes of heat, moisture and CO_2 between the land surface and the atmosphere. Deb Burman et al. (2018) also observed turbulence above the LLJ.

The evaluation of Yang et al. (2017) showed that among several parameters used within PBL and surface-layer parameterization schemes, the Weather Research and Forecasting (WRF) Model is more sensitive to the parameterization of ϵ, contributing for 50% of the variance in an ensemble of forecast runs. Although its importance for the validation of the numerical weather prediction models, the measurements of ϵ are not easily available through the PBL. ϵ can be estimated by different methods, with sonic anemometers, ultrahigh-frequency wind profiling radars (WPR) and Doppler wind lidar data (McCaffrey et al. 2017). As mentioned by McCaffrey et al. (2017), the dissipation rates from sonic anemometers are still estimated, but nowadays they are considered to be true measurements. McCaffrey et al. (2017) describe in detail the method to estimate ϵ from sonic anemometer data. Briefly, ϵ is estimated through the energy spectrum of the wind components (Foken 2008). However, measurements from sonic anemometers are limited by the meteorological tower's height, and applying remote sensing techniques means an advance for the ϵ estimate and consequently for the numerical model parameterizations. McCaffrey et al. (2017) estimated ϵ from two different ultrahigh-frequency WPR (449 and 915 MHz) and proposed a constant to correct the bias in cases when only the WPR data are available. Their strategy nearly removed the entire bias of ϵ. Recent works have shown the benefits of the remote sensing techniques for the comprehension of surface and PBL fluxes within the Earth–atmosphere system and improvement of the numerical weather prediction models (Wulfmeyer et al. 2018; Turner et al. 2018; Wagner et al. 2019). Since 2008 the Doppler lidars have been adopted by the wind energy industry that requires high precision measurements (Peña et al. 2013). That means that in the last decade the Doppler lidars reached the minimum requirements for the wind energy industry needs. The estimate of ϵ with Doppler lidar observations has been demonstrated through recently published articles (Bodini et al. 2018b,a; Banakh and Smalikho 2018; Smalikho and Banakh 2017). Bodini et al. (2018a) verified that ϵ is 12% more variable during nighttime stable conditions than during unstable convective conditions for their experiment at Columbia River Gorge in the northwestern United States, a complex terrain area. Their results suggest that the terrain slope plays an important role in triggering the observed variability of ϵ. The authors concluded that the representation of ϵ in complex terrain, especially during nighttime stable conditions, needs to be extremely localized to capture the turbulence variability in the surface layer.

FIG. 1. Ipero position (red pin)—source: Google Maps.

For this work, we selected one LLJ episode from a 1-yr observational campaign in Ipero, Brazil (Fig. 1). The LLJs are a feature often observed in Ipero and can be explained in terms of the topographic induced flow, despite the synoptic conditions (Oliveira et al. 1995). The wind direction progressively turns counterclockwise due to the inertial oscillation (Fig. 2) and the sloped terrain is the main mechanism of formation of the LLJs in Ipero (Karam et al. 2001). Pereira et al. (2001) showed that the LLJ modulates the atmospheric dispersion for a continuous point source. The daytime concentration field exhibits a typical pattern of homogeneous and stationary conditions and higher concentrations close to the source. The nighttime concentration field is more complex due to the inertial oscillation and topographic blocking effects. Beyond this, the pollutant plume is distorted by the vertical wind shear above and below the LLJ. They verified vertical transport of pollutants from the residual layer to the surface. Pereira et al. (2001) concluded that the LLJ plays an important role for the regional transport of pollutants on a scale of 250 km. Because of its importance for the transport and dispersion of the industrial emissions, the LLJ and their characteristics should be considered for a more realistic dispersion simulation. In this sense, we applied a recently proposed technique by Bodini et al. (2018a) to estimate ϵ for an LLJ event that occurred near the surface in Ipero. We hope these results could improve the understanding of the LLJ role for the atmospheric dispersion and produce more confident dispersion simulations for the industrial sources within the region. The Doppler lidar characteristics, the method to estimate ϵ and the field campaign information are presented in the next section. Sections 3 and 4 present the results and discussion, respectively.

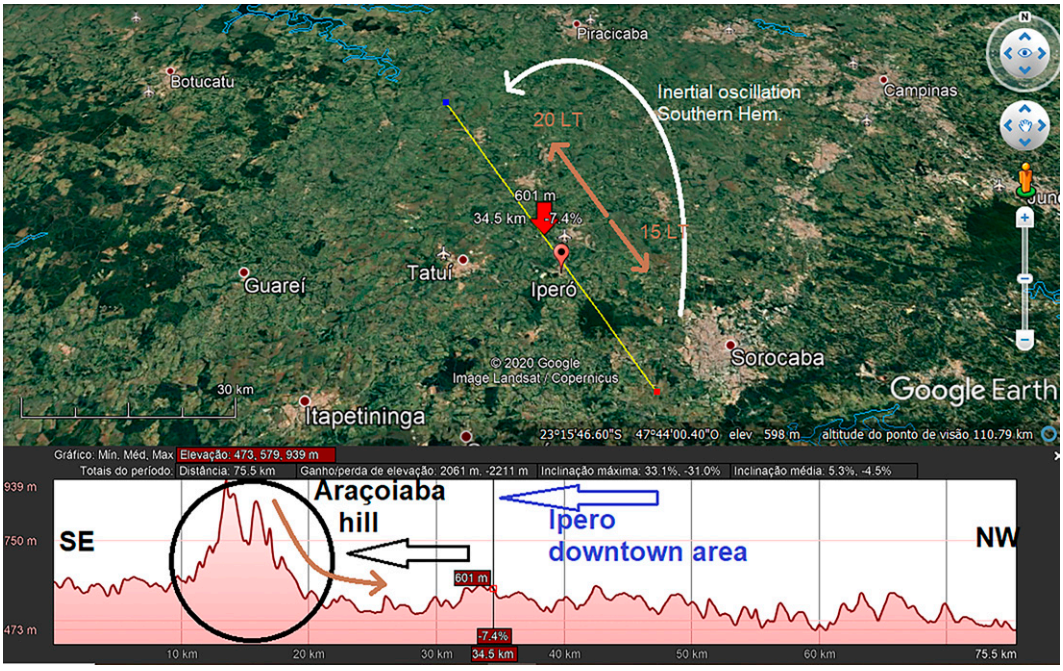

FIG. 2. (top) Ipero (red pin) topographic profile—source: Google Earth. The brown arrows indicate the wind direction at 1500 LT (northwest) and 2000 LT (southeast), and the white arrow indicates the inertial oscillation. (bottom) The brown arrow indicates the flow after 2000 LT, and the black circle highlights Araçoiaba Hill.

2. Materials and methods

a. *Doppler lidar*

For one year, the WindCube, version 2 (v2), Doppler lidar from Leosphere was employed for an observational campaign in Ipero. This campaign, which started in August 2017, was carried out for the next 12 months almost continually. Along this period only few interventions were done for adjustment purposes. From this extensive campaign an observational dataset with more than 340 days is available. The same model of lidar (WindCube v2) has been adopted in other scientific research (Bodini et al. 2018a,b; Bonin et al. 2016; Newman et al. 2016). This is a pulsed lidar with five beams: one beam points out vertically (w component) and the other four beams point out to the cardinal points. Those four beams are inclined 28° from zenith and give the radial velocities V_r for each cardinal point. The main technical specifications of the WindCube v2 are presented on Table 1. For the equation set, see appendix A.

A complete scan lasts around 4 s, but the WindCube v2 algorithm calculates the wind components for every second with the current V_r and the three previous measurements. The lidar was set up for the 12 levels, as follows: 40, 60, 80, 100, 120, 140, 160, 180, 200, 230, 260, and 290 m.

b. *TKE dissipation rate ϵ estimate*

Following Bodini et al. (2018b), we estimated ϵ through this equation:

$$\epsilon = 2\pi\left(\frac{2}{3a}\right)^{3/2}\left(\frac{\sigma_{V_r}^2 - \sigma_e^2}{L^{2/3} - L_1^{2/3}}\right)^{3/2}. \quad (1)$$

Details of this method are found in appendix B. The greatest difficulty of this method is to determine the best value for L, because this parameter depends on the atmospheric stability and the height (O'Connor et al. 2010; Bodini et al. 2018b,a). Bodini et al. (2018b) proposed to adjust a spectral model to the observed spectrum under different stability conditions to determine the ideal wavelength λ_z that separates the inertial subrange from the outer scales, when neither sonic anemometers nor atmospheric stability observations are available. However, to model the radial wind speed spectrum is not a trivial task, once, most of the spectral models are valid for the horizontal and vertical wind components. Bodini et al. (2018a)

TABLE 1. WindCube v2 Doppler lidar technical specifications [adapted from the WindCube manual and Bodini et al. (2018a)].

Characteristic	Value
Min to max height	40–290 m
Time resolution	1 Hz
No. of range gates	12
Vertical resolution	20 m
Wind speed resolution	0.1 m s^{-1}
Wind speed range	0–55 m s^{-1}
Wind direction resolution	2°
Wavelength	1.54 μm
Shot frequency	30 000 Hz
Pulse width	200 ns
Nyquist velocity B	44 m s^{-1}
Signal spectral width Δv	2.65 m s^{-1}
Pulses averaged n	20 000
Points per range gate M	32

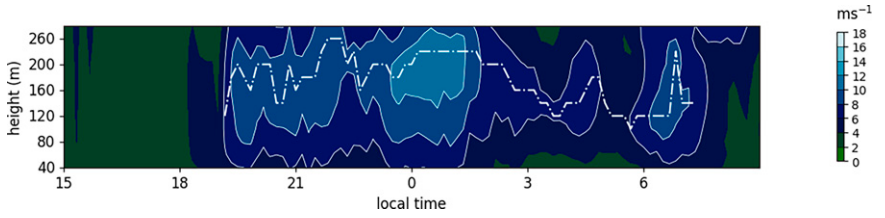

FIG. 3. Wind speed vertical profile starting at 17 Sep. The white dot–dashed line indicates the LLJ height.

overcame that obstacle applying the local regression method to the V_r spectrum.

The first step to estimate ϵ is to determine the length scale L of Eq. (1), where $L = NVt$ (see appendix B, for details). For the WindCube v2 lidar, $t = 1$ s for the V_r profiles. We must determine N, the sample length to be used in the calculations. Bodini et al. (2018b) and Bodini et al. (2018a) showed the importance in determining optimal N for the ϵ estimate through Eq. (1), as L changes with the atmospheric stability and the height.

As in Sanchez Gomez et al. (2021), we determine N from the frequency that gives a power fit with the best agreement with the $f^{-5/3}$ law for the turbulence spectrum. We estimate N for each 15-min interval for the 12 available heights.

For ϵ we take Eq. (1) and the TKE was estimated as the sum of the wind speed component variances according to Stull (1988):

$$\mathrm{TKE} = \frac{1}{2}(\sigma_u^2 + \sigma_v^2 + \sigma_w^2). \tag{2}$$

c. Site

The field campaign took place in Ipero (23°21′S; 47°41′W), a municipality of Sao Paulo State, Brazil. The Fig. 1 shows the Ipero position (red pin) inside the Sao Paulo State, located at the southeastern portion of Brazil, around 120 km from the ocean.

Ipero is located on Medio Tiete River basin, which is oriented from southeast to northwest. Its mean altitude is 600 m, but Araçoiaba Hill at the southeastern portion of Ipero reaches up to 900 m. Ipero is over a transition zone among the rural area, the densely urbanized Sorocaba municipality, and the Ipanema National Forest (a conservation unit).

The topography is shown more detail in Fig. 2, which exhibits the topographic profile along the yellow line over the map for 75 km approximately. Ipero downtown area is in the center of the yellow line. The elevation profile (bottom) highlights Araçoiaba Hill (black circle) and the downtown area (vertical thin line). This elevation profile also shows that the altitude decreases gradually northwestwards, following the Sorocaba–Medio Tiete River basin.

3. Results

Analyzing the 1-yr dataset since August 2017, we found that September had the maximum number of days with LLJs. The LLJs were detected for 28 days [applying the same criteria of Banta et al. (2002)]. For this work we selected the event of 17–18 September, as follows.

a. The 17–18 September LLJ event

Figure 3 illustrates the temporal evolution of the LLJ event of 17–18 September. The horizontal axis is the local time (LT; LT = UTC − 3 h), and the vertical axis is the height. The wind speed is indicated by the legend (m s^{-1}). Winds stronger than 6 m s^{-1} are contoured. At Ipero latitude, the sunset occurs around 1800 LT. The white dot–dashed line indicates the LLJ height H_{LLJ}, identified as the profile's maximum wind speed V_{LLJ}. During the transition time, between 1500 and 1800 LT, the layer through 290 m is homogeneous with weak winds (<4 m s^{-1}). After sunset (1800 LT), we see that wind strengthens, and the LLJ formation is identified around 1900 LT, when the $V_{\mathrm{LLJ}} \geq 5$ m s^{-1} (a criterion we adopted to eliminate weak LLJ events). In the next hours the wind strengthens and the LLJ becomes well defined within the layer between the surface and 290 m. Around 2300 LT the LLJ reaches its strongest intensity and the wind speed exceeds 10 m s^{-1} around 230 m from the surface. After 0200 LT (18 September) the LLJ weakens, its height oscillates within the layer, and the LLJ dissipates only after sunrise (0600 LT). An important feature of this event is how near to the surface this LLJ remained along its life cycle.

The wind direction vertical profile is shown in Fig. 4. As in Fig. 3, the white dot–dashed line indicates the LLJ height. This

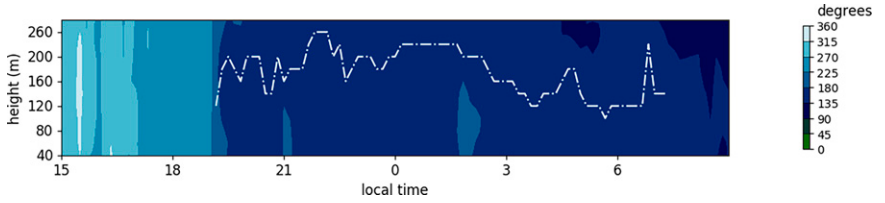

FIG. 4. As in Fig. 3, but for wind direction.

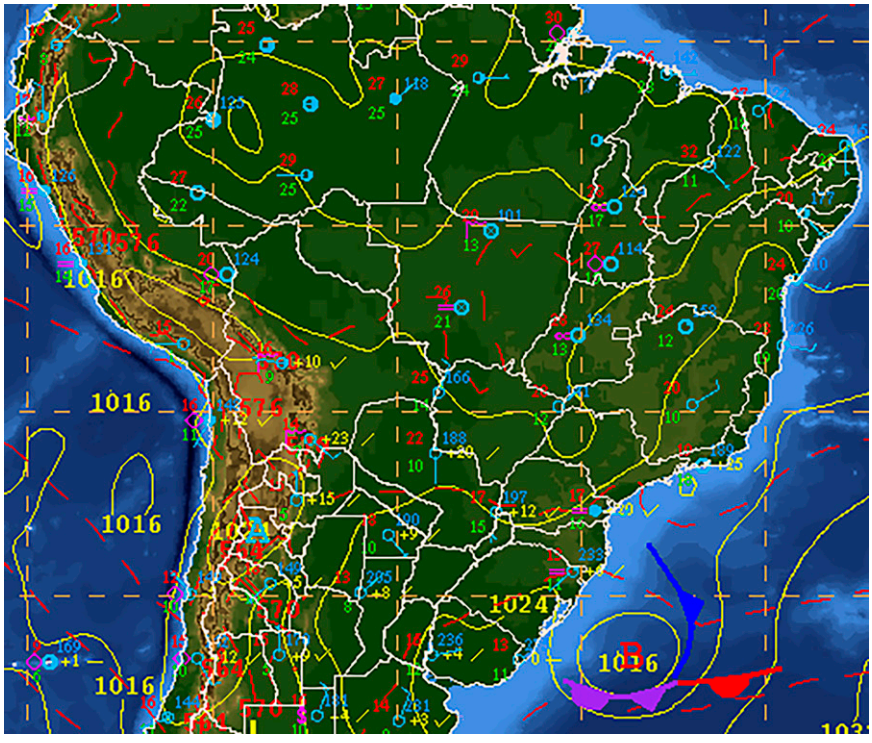

FIG. 5. Synoptic chart for 2100 LT 17 Sep 2017. Source: Centro de Previsão de Tempo e Estudos Climáticos–Instituto Nacional de Pesquisas Espaciais (CPTEC–INPE).

figure shows that the wind direction turns gradually counterclockwise from 1500 LT, but an abrupt change is seen around 1900 LT, when the LLJ is detected for the first time. Then, the wind direction changes from west-southwest to south-southeast (SSE) and remains from SSE until the sunrise. The inertial oscillation is easily seen in the hodographs of 120 and 200 m (see appendix C), which show the wind turning counterclockwise.

For this event, at least, the wind direction remains almost constant through the vertical profile. Other LLJs case studies reported a remarkable directional shear, as mentioned by Banakh and Smalikho (2018) and Smalikho and Banakh (2017).

The LLJ developed under a prefrontal condition, as illustrated in the synoptic chart (Fig. 5) and the satellite imagery (see appendix D), which show a cold front south of Sao Paulo State. The prefrontal condition produced dry and warm advection in Ipero. This synoptic condition inhibited the cloud formation during 12 h before the LLJ formation. Despite the northwestern circulation on the synoptic scale, the local circulation was characterized by weak winds (subgeostrophic). The strongest amplification of the low-level wind occurs on nights after sunny days on which winds in the upper boundary layer were most retarded by surface friction (Markowski and Richardson 2010).

b. *Trajectory and dispersion simulations*

We performed some trajectory and dispersion simulations for this LLJ with the HYSPLIT model (Stein et al. 2015). Something that caught our attention is the fact that the plume can be brought back to the source direction even if the release occurs some hours before the LLJ formation. The trajectory simulations are illustrated in Fig. 6 for releases from 10, 40, and 100 m starting at 0900 LT (17 September), which is 10 h before the LLJ formation. As we see for emissions from 10 and 40 m, the trajectories indicate that the plumes turn back

FIG. 6. HYSPLIT trajectories started with the Global Data Assimilation System (GDAS) 0.5° data at 0900 LT 17 Sep. The heights of release are indicated by the legend.

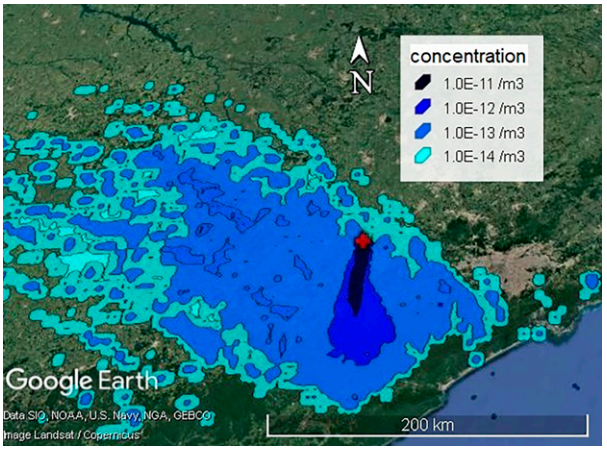

FIG. 7. HYSPLIT relative concentration started with the GDAS 0.5° data at 0900 LT 17 Sep for a 1-h release and 100 arbitrary units per hour of an inert gas. Note that the E in the legend indicates multiplication by 10 raised to the power that follows the E.

to the neighborhoods of their origin, 6 h after the emission, approximately. It can be a combined effect of the sea breeze and LLJ and needs be better studied. In this case, the 100-m release is not affected and follows an almost straight trajectory, but all of the simulations starting between 1200 and 1800 LT (not shown) follow the same pattern (a turn back), including the 100-m release.

As a consequence of the kind of circulation seen for the 10- and 40-m releases, the atmospheric dispersion could be more complex. A simulation with the HYSPLIT model for an inert gas starting at 0900 LT from 10 m showed us that the released material spread widely around the source with highest concentration southerly of the source (Fig. 7). For this simulation we employed an emission rate of 100 arbitrary units per hour for 1 h of emission only. Longer emission time will certainly add complexity to the concentration field. The spread pattern seen in Fig. 7 may complicate the decision making in case of an accidental release of hazardous material and a realistic simulation should be provided for the necessary actions.

c. *Estimating ϵ with the Doppler lidar data*

The ϵ and TKE are shown in Figs. 8 and 9, respectively. As observed by Bodini et al. (2018b), there is a high dependence of ϵ on the wind speed. In their study (Bodini et al. 2018b), ϵ increases one to two orders of magnitude for an increase of 1–15 m s^{-1} in the wind speed. The method of Eq. (1) produced high values of ϵ (Fig. 8 within the layer until 290 m between 1900 and 0100 LT (day + 1), which is the same time interval that the LLJ is stronger (Fig. 3). The ϵ decreases abruptly after the LLJ weakens. We also highlight (i) the order of magnitude (>0.1 m^2 s^{-3}) for wind speed > 8 m s^{-1}, (ii) ϵ spread through the layer (above the LLJ too), (iii) TKE is also observed above the LLJ (Fig. 9), and (iv) maximum TKE and ϵ at different levels.

The high temporal variability of ϵ agrees with results from Smalikho and Banakh (2017), Banakh and Smalikho (2018), Bodini et al. (2018b), and Bodini et al. (2018a). In the Bodini et al. (2018b) study, the temporal series of ϵ changed four orders of magnitude in the same day at 100 m level and typical values of the convective time were observed during the nighttime. This abrupt variation of ϵ was caused by the LLJ formation and as our case study, ϵ decreased as the LLJ weakened. Bodini et al. (2018b) also observed high values of ϵ above the LLJ and Banakh and Smalikho (2018) identified strong ϵ values surrounding the LLJ. The analysis of Bodini et al. (2018a) detected high variability of ϵ and the same magnitude we found in this LLJ case for their work over the complex terrain area of Columbia River Gorge. Beyond this, Bodini et al. (2018a) and Manninen et al. (2018) also verified that there is a seasonal variability of ϵ.

The PBL theory considers the residual layer (RL) as a remaining part of the mixture layer and stationary, where the turbulence vanished (Stull 1988). This concept is adopted by the low-resolution models that consider only large-scale processes as horizontal advection and subsidence (Tjernström et al. 2009). Despite this simplification, Tjernström et al. (2009) affirm that there is an active turbulence within the RL and the laminar flow concept needs to be reviewed. Beyond ϵ and the production and dissipation terms, the TKE budget equation also counts with the transport term, which explains the TKE and ϵ occurrence at different levels (Tjernström et al. 2009).

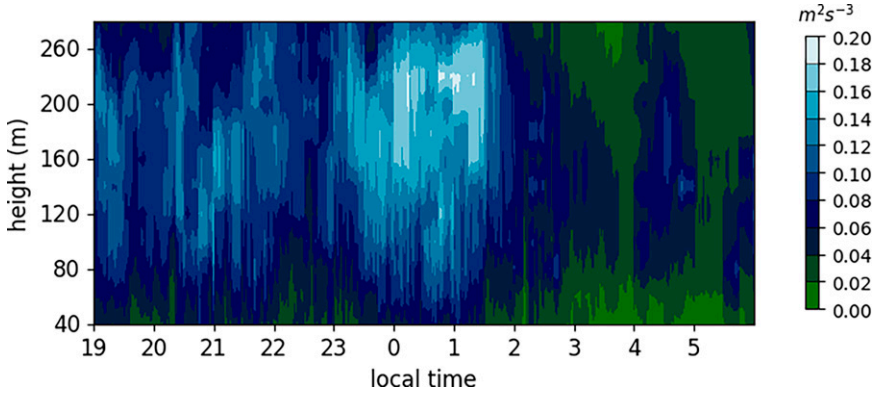

FIG. 8. The spatiotemporal distribution of ϵ.

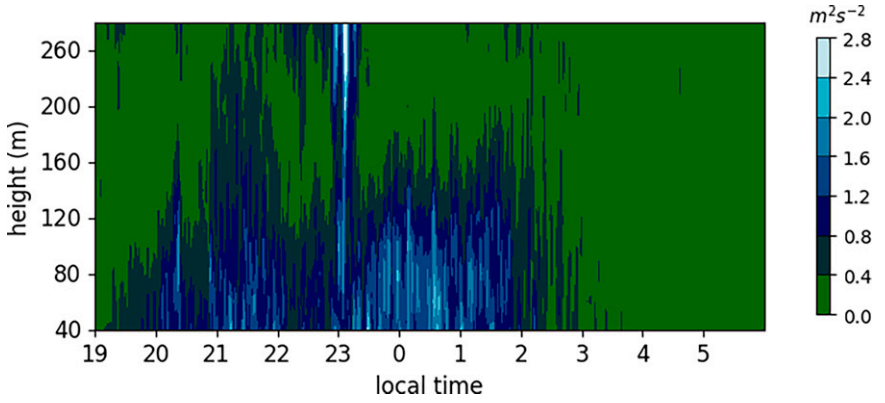

FIG. 9. As in Fig. 8, but for TKE.

Generally, the numerical models assume that the turbulence is generated and dissipated locally, but this hypothesis is appropriate for homogeneous and stationary flow and low-resolution models.

Figure 9 shows that there is a thin channel around 2300 LT that connects the layers below and above the LLJ. Deb Burman et al. (2018) also identified TKE above the LLJ, although, as in our study, the layer below the LLJ is more turbulent and better mixed. This connection between the layer below and above the LLJ may be an exchange channel of their properties, as has been simulated in other studies.

4. Discussion

As a recurrent feature, the LLJ should be considered on the pollutant transport and dispersion over our study area, Ipero. The observational campaign showed us that the LLJs occur with high frequency along the year and form very near the surface (below 300 m). This case study illustrates an LLJ that persisted more than 12 h within the layer below 300-m height.

The innovative method proposed by Bodini et al. (2018a) allows us to estimate the ϵ even if atmospheric stability measurements are not available. This method is especially useful for remote areas where there is not anemometric tower, because the Doppler lidars can be easily transported and operated even at inhospitable sites. Employing Doppler lidar for wind measurements and improving the turbulence estimate techniques is also advantageous from the economic point of view, since to maintain anemometric towers is expensive and operationally laborious and it can demand more workforce. The Doppler lidar, on the turn, offers high spatial resolution and continuous measurements, which are ideal to investigate phenomena within the PBL, especially now that we are seeing the increasing of the wind industry and the development of more sophisticated numerical models that must be correctly parameterized to provide confident simulations.

Our results show that, even for a thin vertical layer, the LLJ produces high spatial and temporal variability of ϵ and that ϵ is highly dependent on the wind speed. The LLJ dynamics through its life cycle implies sudden changes of ϵ. On the contrary to the traditional PBL theory, the ϵ and TKE maximum occur at different levels: while the maximum TKE is near the surface, the maximum ϵ is closer to the LLJ. We also detected TKE above the LLJ and the cause should be investigated in a next work, but as shows the literature, the connection between the layers below and above the LLJ may imply an exchange between these two layers, adding complexity to the mechanisms of pollutant transport and dispersion.

According to the HYSPLIT simulations, the LLJ may interact with another mesoscale circulation feature, such as the sea breeze, and, even under an emergency situation, Gaussian models (e.g., Aloha) should be avoided.

Our extensive field campaign allows us to investigate other LLJ cases and also the seasonality. This certainly will build a strong basis for evaluating the numerical model performance and looking for the best solution for our final goal that is the atmospheric transport and dispersion simulation for industrial emissions.

Acknowledgments. The authors acknowledge the Financiadora de Estudos e Projetos (FINEP) Agency.

Data availability statement. The data are available by request. Please contact author cassia.beu@gmail.com.

APPENDIX A

WindCube v2 Equations

The four V_r estimated for the cardinal points give the following equation set:

$$V_{r1} = v_1 \cos\phi + w_1 \sin\phi, \tag{A1a}$$

$$V_{r2} = u_2 \cos\phi + w_2 \sin\phi, \tag{A1b}$$

$$V_{r3} = -v_3 \cos\phi + w_3 \sin\phi, \text{and} \tag{A1c}$$

$$V_{r4} = -u_4 \cos\phi + w_4 \sin\phi, \tag{A1d}$$

where the subscripts 1, 2, 3 and 4 refer to the cardinal points north, south, east, and west, respectively, and $\phi = 62°$ is the elevation angle from the surface. Assuming a homogeneous flow

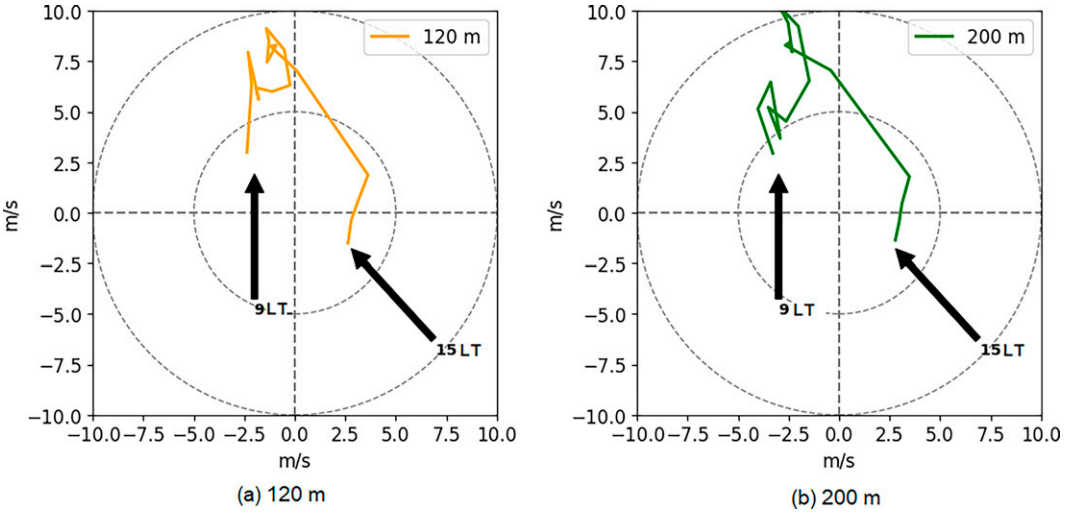

FIG. C1. Hodographs for 120- and 200-m height starting at 1500 LT 17 Sep.

and considering $\overline{u}_2 = \overline{u}_4 = \overline{u}$, $\overline{v}_1 = \overline{v}_3 = \overline{v}$, and $\overline{w}_1 = \overline{w}_2 = \overline{w}_3 = \overline{w}_4 = \overline{w}$, the equation set in Eqs. (A1a)–(A1d) can be resolved for the horizontal wind components

$$\overline{u} = \frac{\overline{V_{r2}} - \overline{V_{r4}}}{2\cos\phi} \quad \text{and} \tag{A2a}$$

$$\overline{v} = \frac{\overline{V_{r1}} - \overline{V_{r3}}}{2\cos\phi}. \tag{A2b}$$

APPENDIX B

Development of the ϵ Equation

Assuming locally homogeneous and isotropic turbulence, the Kolmogorov hypothesis (Foken 2008) establishes that, within the inertial subrange, the one-dimensional spectrum $S(k)$ can be written as

$$S(k) = a\epsilon^{2/3}k^{-5/3}, \tag{B1}$$

where $a = 0.55$ is the Kolmogorov constant and k is the wavenumber related to the length scale L (i.e., $k = 2\pi/L$).

By considering that the wind speed variance σ_V^2 is dominated by turbulent processes and that there are not significative contributions from other sources, the variance can be written as (O'Connor et al. 2010)

$$\sigma_V^2 = \int_k^{k_1} S(k)\,dk. \tag{B2}$$

O'Connor et al. (2010) showed that for Doppler lidars, which generally have very small divergence, $k_1 = 2\pi/L_1$ corresponds to the length scale L_1 of only one sample and that $k = 2\pi/L$ corresponds to the length scale of N samples; $L_1 = Vt$ and $L = NVt$, where V is the horizontal wind speed and t is the time spent to obtain one wind profile.

By integrating Eq. (B2) and replacing k and k_1 with L and L_1,

$$\sigma_V^2 = \frac{3a}{2}\left(\frac{\epsilon}{2\pi}\right)^{2/3}(L^{2/3} - L_1^{2/3}). \tag{B3}$$

Rearranging Eq. (B3), we obtain the expression for ϵ:

$$\epsilon = 2\pi\left(\frac{2}{3a}\right)^{3/2}\left(\frac{\sigma_V^2}{L^{2/3} - L_1^{2/3}}\right)^{3/2}. \tag{B4}$$

O'Connor et al. (2010) estimated ϵ within the convective boundary layer with the vertical wind speed variance σ_w^2 replacing σ_V^2 in Eq. (B4):

$$\epsilon = 2\pi\left(\frac{2}{3a}\right)^{3/2}\left(\frac{\sigma_w^2}{L^{2/3} - L_1^{2/3}}\right)^{3/2}. \tag{B5}$$

This method assumes that the variance is dominated by turbulent processes, but, in truth, there are also contributions from instrumental noise σ_e and the variation in the aerosol terminal fall velocity σ_d; σ_d can be neglected because the particle fall speed is typically very low (<1 cm^{-1}) and its variance σ_d^2 can be safely ignored (O'Connor et al. 2010). Then Eq. (B5) can be rewritten as

$$\epsilon = 2\pi\left(\frac{2}{3a}\right)^{3/2}\left(\frac{\sigma_w^2 - \sigma_e^2}{L^{2/3} - L_1^{2/3}}\right)^{3/2}. \tag{B6}$$

The instrumental noise contribution, in turn, depends on the equipment characteristics, as the laser spectral width, the number of pulses, and the carrier-to-noise ratio CNR. O'Connor et al. (2010) showed that σ_e^2 decreases as the lidar parameters are adjusted for the PBL. Increasing the shot frequency from 15 to 20 kHz and decreasing the integration time from 30 to 4 s, for example, diminished σ_e^2 by

one order of magnitude. As indicated by Table 1, the WindCube v2 lidar presents shot frequency higher (30 kHz) and integration time lower (1 s). The method still assumes that the length scales (L and L_1) are within the inertial subrange. Equation (B6) also presented good results for the stable boundary layer, mainly near the surface.

Bodini et al. (2018b) took the same method [Eq. (B6)], replacing the vertical wind speed variance σ_w^2 by the radial wind speed variance $\sigma_{V_r}^2$, which gives the following expression:

$$\epsilon = 2\pi\left(\frac{2}{3a}\right)^{3/2}\left(\frac{\sigma_{V_r}^2 - \sigma_e^2}{L^{2/3} - L_1^{2/3}}\right)^{3/2}, \tag{B7}$$

Taking $\sigma_{V_r}^2$ means to include the horizontal wind components contribution for the ϵ estimate. The ideal number of samples N depends on the atmospheric stability and the height (Bodini et al. 2018b). The temporal scales that minimized the error for the WindCube v2 relative to the sonic anemometers were 24 s for stable condition and 88 s for unstable condition at 100 m height. Bodini et al. (2018b) also showed that the error decreases under unstable condition and that the temporal scale increases with the height. Among the three Doppler lidars analyzed in their research, the WindCube v2 was the one that produced the best results relative to the sonic anemometers. According to Bodini et al. (2018b), the possible discrepancy sources are the different temporal resolution and the sampling volume for each equipment, but the estimate obtained with the refinement of the method of O'Connor et al. (2010) is robust.

The error due to the instrumental noise σ_e^2 is given by O'Connor et al. (2010) and Bodini et al. (2018b):

$$\sigma_e^2 = \frac{\Delta v^2\sqrt{8}}{\alpha N_p}\left(1 + \frac{\alpha}{\sqrt{2\pi}}\right)^2, \tag{B8}$$

where

$$\alpha = \frac{\mathrm{CNR}}{\sqrt{2\pi}}\frac{B}{\Delta v} \quad \text{and} \tag{B9}$$

$$N_p = \mathrm{CNR} \times n \times M. \tag{B10}$$

In Eqs. (B8), (B9), and (B10), Δv, B, n, and M, are respectively the signal spectral width, the Nyquist velocity, the pulses averaged, and the points per range gate (Table 1).

APPENDIX C

Hodographs

Figure C1 presents the hodographs for 120- and 200-m height, showing the wind turning counterclockwise.

APPENDIX D

Satellite Imagery

Figure D1 presents *GOES-13* satellite imagery, showing a cold front south of Sao Paulo State.

FIG. D1. *GOES-13* satellite imagery at 2100 LT 17 Sep 2017.

REFERENCES

Allen, C. J., and R. Washington, 2014: The low-level jet dust emission mechanism in the central Sahara: Observations from Bordj-Badji Mokhtar during the June 2011 Fennec intensive observation period. *J. Geophys. Res. Atmos.*, **119**, 2990–3015, https://doi.org/10.1002/2013JD020594.

Banakh, V. A., and I. N. Smalikho, 2018: Lidar studies of wind turbulence in the stable atmospheric boundary layer. *Remote Sens.*, **10**, 1219, https://doi.org/10.3390/rs10081219.

Banta, R. M., and Coauthors, 1998: Daytime buildup and nighttime transport of urban ozone in the boundary layer during a stagnation episode. *J. Geophys. Res.*, **103**, 22 519–22 544, https://doi.org/10.1029/98JD01020.

——, R. K. Newsom, J. K. Lundquist, Y. Pichugina, R. L. Coulter, and L. Mahrt, 2002: Nocturnal low-level jet characteristics over Kansas during CASES-99. *Bound.-Layer Meteor.*, **105**, 221–252, https://doi.org/10.1023/A:1019992330866.

——, Y. L. Pichugina, and W. A. Brewer, 2006: Turbulent velocity-variance profiles in the stable boundary layer generated by a nocturnal low-level jet. *J. Atmos. Sci.*, **63**, 2700–2719, https://doi.org/10.1175/JAS3776.1.

Bodini, N., J. K. Lundquist, R. Krishnamurthy, M. Pekour, and L. K. Berg, 2018a: Spatial and temporal variability of turbulence dissipation rate in complex terrain. *Atmos. Chem. Phys. Discuss.*, **1**, 1–27, https://doi.org/10.5194/acp-2018-1131.

——, ——, and R. K. Newsom, 2018b: Estimation of turbulence dissipation rate and its variability from sonic anemometer and wind Doppler lidar during the XPIA field campaign. *Atmos. Meas. Tech.*, **11**, 4291–4308, https://doi.org/10.5194/amt-11-4291-2018.

Bonin, T. A., W. G. Blumberg, P. M. Klein, and P. B. Chilson, 2015: Thermodynamic and turbulence characteristics of the southern Great Plains nocturnal boundary layer under differing turbulent regimes. *Bound.-Layer Meteor.*, **157**, 401–420, https://doi.org/10.1007/s10546-015-0072-2.

——, J. F. Newman, P. M. Klein, P. B. Chilson, and S. Wharton, 2016: Improvement of vertical velocity statistics measured by a Doppler lidar through comparison with sonic anemometer observations. *Atmos. Meas. Tech.*, **9**, 5833–5852, https://doi.org/10.5194/amt-9-5833-2016.

Darby, L. S., K. J. Allwine, and R. M. Banta, 2006: Nocturnal low-level jet in a mountain basin complex. Part II: Transport and diffusion of tracer under stable conditions. *J. Appl. Meteor. Climatol.*, **45**, 740–753, https://doi.org/10.1175/JAM2367.1.

Deb Burman, P. K., T. V. Prabha, R. Morrison, and A. Karipot, 2018: A case study of turbulence in the nocturnal boundary layer during the Indian summer monsoon. *Bound.-Layer Meteor.*, **169**, 115–138, https://doi.org/10.1007/s10546-018-0364-4.

Foken, T., 2008: *Micrometeorology*. Springer, 306 pp.

Jia, S., F. Melvin, L. Liqiao, M. M. Patrick, D. Ruben, and S. P. Alexandra, 2016: Lidar remote sensing of cloud formation caused by low-level jets. *J. Geophys. Res. Atmos.*, **121**, 5904–5911, https://doi.org/10.1002/2015JD024590.

Karam, H. A., A. P. Oliveira, and M. M. R. Pereira, 2001: Application of a Lagrangian model to investigate patterns of radionuclides dispersion over complex terrain—Part 1: Local circulation and low-level jet. *Proc. Seventh Int. Conf. on Harmonisation within Atmospheric Dispersion Modelling for Regulatory Purposes*, Belgirate, Italy, HARMO, 395–399.

Manninen, A. J., T. Marke, M. Tuononen, and E. J. O'Connor, 2018: Atmospheric boundary layer classification with Doppler lidar. *J. Geophys. Res. Atmos.*, **123**, 8172–8189, https://doi.org/10.1029/2017JD028169.

Markowski, P. M., and Y. P. Richardson, 2010: *Mesoscale Meteorology in Midlatitudes*. Wiley-Blackwell, 430 pp.

McCaffrey, K., L. Bianco, and J. M. Wilczak, 2017: Improved observations of turbulence dissipation rates from wind profiling radars. *Atmos. Meas. Tech.*, **10**, 2595–2611, https://doi.org/10.5194/amt-10-2595-2017.

Newman, J. F., P. M. Klein, S. Wharton, A. Sathe, T. A. Bonin, P. B. Chilson, and A. Muschinski, 2016: Evaluation of three lidar scanning strategies for turbulence measurements. *Atmos. Meas. Tech.*, **9**, 1993–2013, https://doi.org/10.5194/amt-9-1993-2016.

Nobre, C. A., J. A. Marengo, and P. Artaxo, 2013: Understanding the climate of Amazonia: Progress from LBA. *Amazonia and Global Change*, *Geophys. Monogr.*, Vol. 186, Amer. Geophys. Union, 145–147, https://doi.org/10.1029/2008GM000716.

O'Connor, E. J., A. J. Illingworth, I. M. Brooks, C. D. Westbrook, R. J. Hogan, F. Davies, and B. J. Brooks, 2010: A method for estimating the turbulent kinetic energy dissipation rate from a vertically pointing Doppler lidar, and independent evaluation from balloon-borne in situ measurements. *J. Atmos. Oceanic Technol.*, **27**, 1652–1664, https://doi.org/10.1175/2010JTECHA1455.1.

Oliveira, A. P., G. A. Degrazia, O. L. L. Moraes, and T. Tirabassi, 1995: Numerical study of the nocturnal planetary boundary layer at low latitudes. *Trans. Ecol. Environ.*, **9**, 167–174.

Peña, A., and Coauthors, 2013: *Remote Sensing for Wind Energy*. DTU Wind Energy, 260 pp.

Pereira, M. M. R., A. P. Oliveira, and H. A. Karam, 2001: Application of a Lagrangian model to investigate patterns of radionuclides dispersion over complex terrain—Part 2: The impact of the low-level jet in the concentration field. *Proc. Seventh Int. Conf. on Harmonisation within Atmospheric Dispersion Modelling for Regulatory Purposes*, Belgirate, Italy, HARMO, 400–404.

Sanchez Gomez, M., J. K. Lundquist, P. M. Klein, and T. M. Bell, 2021: Turbulence dissipation rate estimated from lidar observations during the LAPSE-RATE field campaign. *Earth Syst. Sci. Data*, **13**, 3539–3549, https://doi.org/10.5194/essd-13-3539-2021.

Smalikho, I. N., and V. A. Banakh, 2017: Measurements of wind turbulence parameters by a conically scanning coherent Doppler lidar in the atmospheric boundary layer. *Atmos. Meas. Tech.*, **10**, 4191–4208, https://doi.org/10.5194/amt-10-4191-2017.

Stein, A., R. Draxler, G. Rolph, B. Stunder, M. D. Cohen, and F. Ngan, 2015: NOAA's HYSPLIT atmospheric transport and dispersion modeling system. *Bull. Amer. Meteor. Soc.*, **96**, 2059–2077, https://doi.org/10.1175/BAMS-D-14-00110.1.

Stull, R. B., 1988: *An Introduction to Boundary Layer Meteorology*. Kluwer Academic, 666 pp.

Sullivan, J. T., S. D. Rabenhorst, J. Dreessen, T. J. McGee, R. Delgado, L. Twigg, and G. Sumnicht, 2017: Lidar observations revealing transport of O_3 in the presence of a nocturnal low-level jet: Regional implications for "next-day" pollution. *Atmos. Environ.*, **158**, 160–171, https://doi.org/10.1016/j.atmosenv.2017.03.039.

Tjernström, M., B. B. Balsley, G. Svensson, and C. J. Nappo, 2009: The effects of critical layers on residual layer turbulence. *J. Atmos. Sci.*, **66**, 468–480, https://doi.org/10.1175/2008JAS2729.1.

Turner, D. D., V. Wulfmeyer, A. Behrendt, T. A. Bonin, A. Choukulkar, R. K. Newsom, W. A. Brewer, and D. R. Cook, 2018: Response of the land-atmosphere system over north-central Oklahoma during the 2017 eclipse. *Geophys. Res. Lett.*, **45**, 1668–1675, https://doi.org/10.1002/2017GL076908.

Wagner, T. J., P. M. Klein, and D. D. Turner, 2019: A new generation of ground-based mobile platforms for active and passive profiling of the boundary layer. *Bull. Amer. Meteor. Soc.*, **100**, 137–153, https://doi.org/10.1175/BAMS-D-17-0165.1.

Wulfmeyer, V., and Coauthors, 2018: A new research approach for observing and characterizing land–atmosphere feedback. *Bull. Amer. Meteor. Soc.*, **99**, 1639–1667, https://doi.org/10.1175/BAMS-D-17-0009.1.

Yang, B., and Coauthors, 2017: Sensitivity of turbine-height wind speeds to parameters in planetary boundary-layer and surface-layer schemes in the weather research and forecasting model. *Bound.-Layer Meteor.*, **162**, 117–142, https://doi.org/10.1007/s10546-016-0185-2.